JOURNAL OF GEOPHYSICAL RESEARCH, VOL. 102, NO. D14, PAGES 16,911–16,922, JULY 27, 1997

Global distribution of UV-absorbing aerosols from Nimbus 7/TOMS data

J. R. Herman and P. K. Bhartia
Laboratory for Atmospheres, Goddard Space Flight Center, Greenbelt, Maryland

O. Torres, C. Hsu, and C. Seftor
Hughes STX Corporation, Greenbelt, Maryland

E. Celarier
Software Corporation of America, Lanham, Maryland

Abstract. Global distributions of UV-absorbing aerosols are obtained using measured differences between the 340 and the 380 nm radiances from the Nimbus 7 Total Ozone Mapping Spectrometer (TOMS) for the years 1979–1993. Time series are shown for major sources of biomass burning and desert dust giving the frequency of occurrence and areal coverage over land and oceans. Minor sources of UV-absorbing aerosols in the atmosphere are also discussed (volcanic ash and oil fires). Relative values of year-to-year variability of UV-absorbing aerosol amounts are shown for major aerosol source regions: (1) central South America (Brazil) near 10°S latitude; (2) Africa near 0°–20°S and 0° to 10°N latitude; (3) Saharan Desert and sub-Saharan region (Sahel), Arabian Peninsula, and the northern border region of India; (4) agricultural burning in Indonesia, Eastern China, and Indochina, and near the mouth of the Amazon River; and (5) coal burning and dust in northeastern China. The first three of these regions dominate the injection of UV-absorbing aerosols into the atmosphere each year and cover areas far outside of their source regions from advection of UV-absorbing particulates by atmospheric wind systems. During the peak months, smoke and dust from these sources are transported at altitudes above 1 km with an optical depth of at least 0.1 and can cover about 10% of the Earth's surface. Boundary layer absorbing aerosols are not readily seen by TOMS because the small amount of underlying Rayleigh scattering leads to a small signal. Significant portions of the observed dust originate from agricultural regions frequently within arid areas, such as in the Sahel region of Africa, especially from the dry lake-bed near Lake Chad (13.5°N, 14°E), and intermittently dry drainage areas and streams. In addition to drought cycle effects, this suggests there may be an anthropogenic component to the amount of dust injected into the atmosphere each year. Detection of absorbing aerosols and calculation of optical depths are affected by the presence of large-scale and subpixel clouds in the TOMS field of view.

Introduction

The presence of UV-absorbing aerosols in the atmosphere affects both the radiation balance [*Haywood and Shine*, 1995; *Ardanuy et al.*, 1992] and the amount of UV flux reaching the ground. The atmospheric loading of UV-absorbing aerosols is the sum of several large annually cyclic sources of aerosols distributed over large areas by tropospheric wind circulation. Observations of UV-absorbing aerosols at sites remote from the sources also show a distinct cyclic pattern [*Bodhaine*, 1995] driven by atmospheric transport from one or more of these sources. Smoke plumes, desert dust, and volcanic ash have been observed from satellite data in the visible and IR channels of AVHRR (advanced very high resolution radiometer) and GOES (Geostationary Operational Environmental Satellite) system [*Matson and Holben*, 1987; *Holben et al.*, 1991; *Robinson*, 1991; *Kaufman et al.*, 1992; *Prins and Menzel*, 1992; *Wen and Rose*, 1994; *Husar et al.*, this issue]. For the most part, the AVHRR observations are limited to being over water because of requirements for low, nonvariable surface reflectivity that are not met over land.

In this paper we present results from a new technique for detecting UV-absorbing aerosols in the atmosphere from the spectral contrast (ratio of 340–380 nm radiances, I_{340}/I_{380}) between the 340 and the 380 nm channels of the total ozone mapping spectrometer (TOMS) that flew on the Nimbus 7 satellite from November 1978 to May 1993 [*McPeters et al.*, 1996]. Although the results are restricted in this paper to UV-absorbing aerosols, such as smoke, desert dust, and volcanic ash, clouds and nonabsorbing aerosols are also detected in the TOMS spectral contrast data. In addition, the UV spectral contrast method does not suffer from the limitation of the visible-wavelength techniques, since the UV surface reflectivity is low and nearly constant over both land and water.

The next section provides background information on TOMS, including the concept of residue that is central to the

Paper number 96JD03680.
0148-0227/97/96JD-03680$09.00

detection of aerosols from TOMS. This is followed by a brief summary of the radiative transfer calculations that relates reflectivity residues observed by TOMS to aerosol parameters. Later sections present highlights of the aerosol signals detected in the multiyear TOMS data set on daily to long-term timescales.

Background

The Nimbus 7/TOMS [*Heath et al.*, 1975] measured the amount of backscattered UV radiance in six 1 nm wide wavelength bands (313, 318, 331, 340, 360, and 380 nm). During its unprecedented 14.5 year lifetime, TOMS took measurements almost every single day, over most of the Earth's surface (except regions in polar night). The data were taken in a series of scans, perpendicular to the TOMS near-polar orbit (13.8 Sun-synchronous orbits per day with near-noon equator crossing time). Each side scan, consisting of 35 samples, covered an angular range of ±51° about the nadir. The scan rate and angular swath were designed to provide contiguous coverage of the entire globe. The second non-Sun-synchronous TOMS instrument operated on the Russian Meteor 3 satellite from August 1991 to December 1994 [*Herman and Larko*, 1994]. A modified version of the previous two instruments, EP/TOMS, was launched on July 2, 1996, aboard NASA's Earth-Probe (EP) satellite into a Sun-synchronous low-altitude orbit designed for better detection of absorbing aerosols. During August 1996, ADEOS/TOMS was launched in a higher orbit with spatial resolution similar to Nimbus 7/TOMS. Additional flights of TOMS or TOMS-like instruments are planned over the next decade.

Meteor 3/TOMS was in operation from August 1991 to December 1994, but its orbit precesses from the sunrise terminator to the sunset terminator every 106 days. When the orbit of Meteor 3/TOMS is close to the near-noon orbit of Nimbus 7/TOMS, the data quality is comparable both in ozone amount and in aerosol detection. Because of the precessing orbit of Meteor 3/TOMS, this study considers only the Sun-synchronous Nimbus 7/TOMS data.

The TOMS instrument was designed to provide accurate global estimates of total column ozone, and can detect SO_2 [*Krueger et al.*, 1995], estimate surface ultraviolet amounts [*Herman et al.*, 1996], and detect H_2SO_4 stratospheric aerosols [*Torres et al.*, 1995]. The inversion method for obtaining ozone amounts relies on accurate separation of the wavelength dependence of backscattered radiation due to ozone absorption from that due to atmospheric scattering. The three longest wavelength bands (340, 360, and 380 nm) of TOMS were provided to test different models of the atmosphere in reproducing the observed wavelength dependence of the backscattered radiation. Since gaseous absorption at these wavelengths is weak, the backscattered radiation is primarily controlled by molecular (Rayleigh) scattering, surface reflection, and (Mie) scattering from aerosols and clouds.

Early results from satellite measurements showed that an atmospheric model proposed by *Dave* [1978], the Lambert equivalent reflectivity (LER) model, reproduced the wavelength dependence of the observed radiation in a large variety of observing conditions. In Dave's LER model, the atmosphere consists of Rayleigh scatterers bounded by a Lambertian surface whose reflectivity R is estimated from the measured radiances [*Bhartia et al.*, 1993]. For a pure Rayleigh atmosphere, R is an approximation of the value of the bidirectional reflectivity distribution function (BRDF) of the surface at a given measurement geometry [*Dave*, 1965]. The difference between R and BRDF is caused by the mixing of reflecting angles due to molecular scattering. Since this mixing depends on the strength of the wavelength dependent molecular scattering, R also becomes wavelength dependent in the presence of highly non-Lambertian surfaces, e.g., sea glint and snow/ice. Data containing sea glint were edited out of this analysis using the measurement geometry to determine its occurrence. The high-reflectivity effects of snow/ice were minimized by restricting the analysis to between the latitudes of ±60°.

In the presence of clouds and aerosols, R is greater than the BRDF of the surface except when significant amounts of highly UV-absorbing aerosols are present. Analysis of TOMS data shows that Mie scattering can also make R spectrally dependent. The effect is most pronounced for UV-absorbing aerosols, which causes R to increase with wavelength [*Hsu et al.*, 1996]. Nonabsorbing aerosols/clouds, under certain conditions, can cause R to decrease with wavelength ($R_{380} < R_{340}$). Nonabsorbing aerosols produce effects similar (though not necessarily identical) to thin clouds, so that residues for such aerosols are close to zero. Second-order effects related to the fact that aerosol size distribution is different from those of clouds can produce small positive and negative residues. A modification to the ozone retrieval algorithm [*McPeters et al.*, 1996] was implemented that used the wavelength dependence of R to reject data that are highly contaminated by dust or smoke in the field of view and to correct moderately contaminated data.

The level-2 TOMS data sets available from Goddard Space Flight Center Distributed Active Archive Center (GSFC/DAAC), Greenbelt, Maryland, contain N-value residues at the wavelength $\lambda = 340$ nm defined as

$$\Delta N_\lambda = -100 \log_{10} [(I_{340})_{meas}/(I_{340})_{calc}] \quad (1)$$

Since R is determined by requiring $(I_{380})_{meas} = (I_{380})_{calc}$, ΔN_λ can be expressed in terms of the radiance contrast I_{340}/I_{380}.

$$\Delta N_\lambda = -100\{\log_{10}[(I_{340}/I_{380})_{meas}] - \log_{10}[(I_{340}/I_{380})_{calc}]\} \quad (2)$$

where I_{meas} is the measured backscattered radiance at a given wavelength and I_{calc} is the radiance calculated at that wavelength using a modified version of Dave's LER model [*McPeters et al.*, 1996]. The model is constructed to give nearly zero residue at all TOMS wavelengths in the presence of clouds by reproducing an average observed spectral contrast for clouds. As shown later, this formulation produces good separation between the presence of absorbing aerosols and clouds and so can be used for aerosol imaging and quantitative calculations of optical depth and single-scattering albedo.

Detection of Aerosols in UV

In principle, there are two independent methods for detecting aerosols and clouds from the backscattered ultraviolet (BUV) radiance measurements in the 340–380 nm range, the single-channel and multichannel spectral contrast methods. A modified form of the spectral contrast method, the residue method, is used for TOMS.

The most direct method, similar to the one used by instruments operating in the visible, such as the AVHRR, is to estimate aerosols/cloud scattering optical thickness from the

increase in the BUV radiation from its background value at a single wavelength. The principle advantage of UV over visible wavelengths is that the UV reflectivity of the Earth's surface (not covered with snow/ice) is typically very small [*Eck et al.*, 1987], therefore clouds and aerosols can be detected over both land and ocean. This method was used to develop a multiyear cloud climatology by combining TOMS data with the temperature and humidity infrared radiometer (THIR) instrument on the Nimbus 7 satellite [*Stowe et al.*, 1985]. Compared to the visible, the BUV radiances are more sensitive to absorbing aerosols because absorption not only attenuates aerosol scattering but also molecular scattering from the atmosphere in and below the aerosol layer. For TOMS the principal difficulty in detecting aerosols using this method is the large field of view of the TOMS instrument (50 × 50 km at nadir, 150 × 250 km at extreme off nadir), which almost always contains subpixel clouds. The subpixel cloud problem can be minimized by using more than one wavelength channel.

An alternate technique can be used to detect clouds and aerosols by looking at the spectral contrast of two UV channels (we used 340 and 380 nm, since the 360 nm channel includes a strong Raman scattering component [*Joiner et al.*, 1995]). In a clear molecular atmosphere with low surface reflectivities, the λ^{-4} wavelength dependence of molecular scattering produces up to 50% difference in the BUV radiances between 340 and 380 nm. Since aerosols and clouds typically add a radiance component that is weakly wavelength dependent, they reduce the I_{340}/I_{380} spectral contrast. By monitoring the reduction in the spectral contrast, one can detect the presence of Mie scatterers. However, this method suffers from the same cloud/aerosol discrimination problem as before, for they both reduce spectral contrast.

Key to the TOMS aerosol detection technique is the realization that by combining two independent pieces of information, namely, the I_{340}/I_{380} spectral contrast and the change in backscattered 380 nm radiance, one can detect the presence of absorbing and nonabsorbing particulates embedded in a Rayleigh scattering atmosphere with the effects of clouds on spectral contrast removed by using the LER model. Radiative transfer calculations show that for a fixed change in 380 nm radiance the I_{340}/I_{380} spectral contrast depends strongly on the absorption optical thickness of the Mie scatterers, given by $\tau(1 - \omega_o)$, where τ is the total optical thickness and ω_o is the single-scattering albedo. The spectral contrast for a fixed 380 nm radiance is largest for nonabsorbing aerosols/clouds and decreases with increasing absorption. UV-absorbing aerosols produce smaller contrast than predicted from the LER model and hence produce positive residues. Nonabsorbing aerosols produce greater contrast and negative residues. One of the unique strengths of this technique is that since clouds produce nearly zero residue, the presence of subpixel clouds does not affect the detection of aerosols. However, the amount of aerosols detected would be reduced because of obscuration of the aerosol layer by clouds.

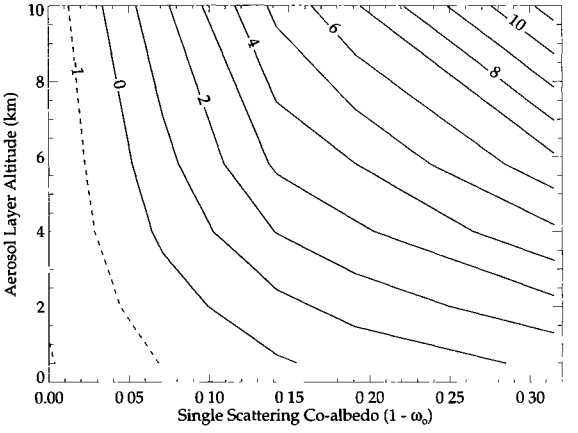

Figure 1. Contour plot of the radiance residue ΔN_{340} for a geometrically thin aerosol layer of optical depth $\tau_{380} = 1$ (solar zenith angle = 40°, surface reflectivity = 2%) as a function of layer altitude and the aerosol coalbedo $C(\omega_o) = (1 - \omega_o)$. The detection sensitivity for strongly UV-absorbing aerosols increases with the altitude of the aerosol layer but decreases slightly with increasing altitude for weakly UV-absorbing and nonabsorbing aerosols. For strongly UV-absorbing aerosols the detection sensitivity increases with $C(\omega_o)$.

Figure 1 and Table 1 summarize some of the results of detailed Mie scattering calculations that we have performed to understand the aerosol information in the TOMS radiances (O. Torres et al., manuscript in preparation, 1996). The figure shows the contours of the 340 nm N-value residue ΔN_{340}, for aerosols of total optical thickness $\tau = 1$, as a function of single-scattering albedo and aerosol altitude. From radiative transfer calculations (also see Table 1), ΔN_{340} values scale approximately linearly with optical thickness. Dependence on other aerosol parameters, e.g., size distribution, mean particle size, real part of the refractive index, is smaller than that for optical depth and altitude. For strongly UV-absorbing aerosols, ΔN_{340} has a strong altitude dependence arising from the effects of aerosol absorption on molecular scattering originating below the aerosol layer. While this interaction is essential for the aerosol detection method to work, it also means that UV-absorbing aerosols in the boundary layer near the ground cannot readily be detected by this method because the signal is weak relative to the apparent noise from the ground. At altitudes of about 1 km, absorbing aerosols become easily detect-

Table 1. N-Value Residue, ΔN_{340}, for Absorbing Aerosols, Nadir View, and Overhead Sun

$k = 0.04$, $\tau_{380} = 1$ $h = 2.9$ km		$r_{eff} = 0.1$, $\tau_{380} = 1$ $h = 2.9$ km		$k = 0.04$, $\tau_{380} = 1$ $h = 2.9$ km		$r_{eff} = 0.1$, $k = 0.04$ $r_{eff} = 0.1$	
Particle Size, μm	ΔN_{340}	Absorbing Index, k	ΔN_{340}	Height, km	ΔN_{340}	Optical Depth, τ	ΔN_{340}
0.1	2.06	0.02	0.71	1.4	0.94	0.1	0.54
0.2	3.03	0.04	2.06	2.9	2.06	0.5	1.32
0.8	5.07	0.06	2.97	5.8	4.18	1.0	2.06

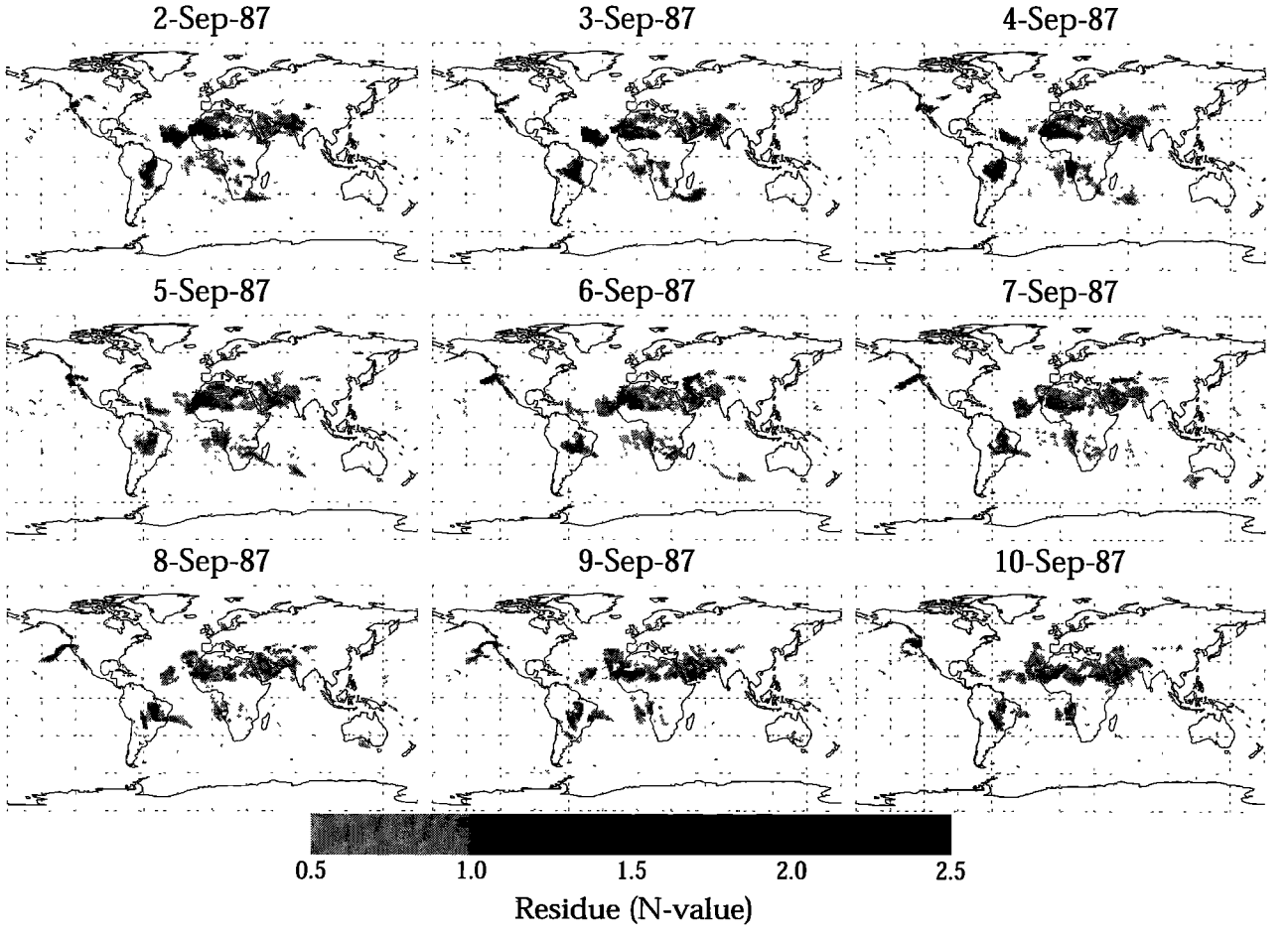

Figure 2. Aerosol N-value residues for September 2, 1987, to September 10, 1987, showing biomass burning and desert dust transported by prevailing winds in the lower troposphere.

able from the background signal. At middle latitudes the aerosols can be detected since most of the aerosol transport is in the free troposphere at 3–5 km altitude or higher (e.g., volcanic ash).

The range of appropriate single-scattering albedos used in Figure 1 is calculated from refractive indices obtained from *Patterson and McMahon* [1984] (smoke refractive index), *Patterson et al.* [1977] (desert dust refractive index), and *Patterson* [1981] and *Patterson and Pollard* [1983] (volcanic ash refractive index). Similarly, the parameters for the lognormal particle size distribution were taken from *Westphal and Toon* [1991], *Westphal et al.* [1989], and *D'Almeida* [1987] for smoke and dust, respectively.

It is important to note that the results shown in Figure 1 are calculated for "gray" aerosols, i.e., with refractive indices that are wavelength independent. This means that aerosol radiance residues ΔN_{340} are not caused by differences in optical properties of the aerosols at 340 and 380 nm wavelengths but are the result of interaction between the aerosol scattering and the strongly wavelength dependent Rayleigh scattering.

In the subsequent sections we present maps of UV-absorbing aerosols. There are basically two kinds of absorbing aerosols present in these maps: desert dust and smoke. The radiance residues resulting from both of these types of aerosols are roughly comparable on the TOMS global maps. However, the estimated absorption optical depths can be different since TOMS residues are a measure of the product of the absorption optical thickness and single-scattering coalbedo and are less sensitive to the nonabsorbing component of the aerosol extinction. Since dust particle plumes tend to have a larger mean radius than smoke particle plumes, their single-scattering albedos are larger and optical depths smaller for the same value of the residue. Negative residues are omitted in this study so that nonabsorbing aerosols (e.g., sulfate aerosols) are not shown. Except for Figures 2 and 3, all of the map pixels have a lower limit of +1 N-value residue unit to be considered to contain absorbing aerosol. Below +0.5 N-value units of residue, the observation may contain a ground signal, nonabsorbing aerosol signal, or noise.

Daily Aerosol Measurements

Examples for nine successive days (September 2–10, 1987) of UV-absorbing aerosols distributed over the entire globe are given in Figure 2. The results, expressed in positive 340 nm residues (defined in equations (1) and (2)), show biomass burning in southern Africa in the latitude range 1°S to 20°S, South America near 10°S (Brazil), and North America (California-Oregon border near 42°N 124°W), as well as a dust storm originating near 15°N latitude in North Africa in the Sahel and transported over the Atlantic Ocean, the Arabian Peninsula, and northern India. The biomass burning in South America and southern Africa show the effect of lower tropo-

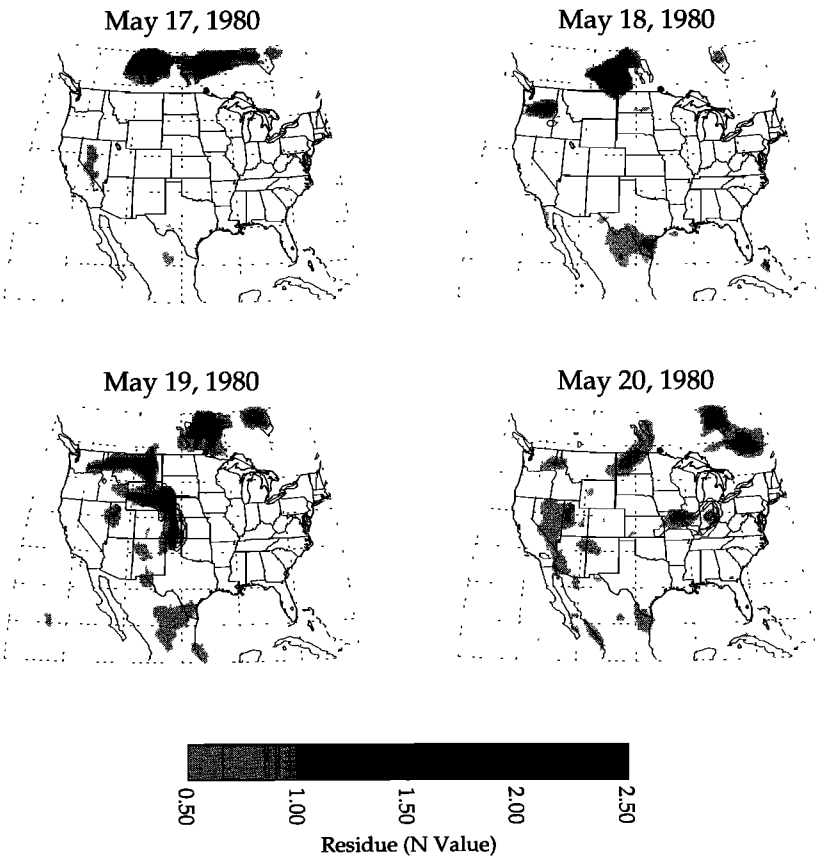

Figure 3. *N*-value residue caused by UV-absorbing aerosols and SO_2 (contour lines) from the eruption of Mount St. Helens on May 17, 1980, to May 20, 1980. By coincidence the figure also shows the smoke from Canadian forest and brush fires that occurs most years as a result of ignition from lightning, and in addition, dust clouds over Mexico and the southwestern United States.

spheric wind transport on smoke plumes. Depending on the point of origin in southern Africa, the smoke plumes are carried either westward over the Atlantic or eastward over the Indian Ocean. On most days of the year, desert dust blows westward off the Saharan Desert and Sahel region over the Atlantic Ocean (on many days reaching Cuba and Florida and can cover the Caribbean basin and southeastern United States). An interesting feature is visible on September 8, 9, and 10, where the dust flows northward from Africa over the Atlantic west of Spain. On other days (not shown), dust from Africa is seen over Spain and the Mediterranean. In North America, Figure 2 shows smoke from two fires originating in the western United States, with smoke from one carried northeastward and the other westward over the Pacific Ocean. The northeast plume turns around in a few days and flows westward over the Pacific Ocean.

A second example is given in Figure 3 showing the short-lived (less than 10 days) injection of volcanic ash and SO_2 into the troposphere after the eruption of Mount St. Helens in Washington State on May 17, 18, 19, and 20, 1980. On the day before the May 17, 1980 eruption, the area near Mount St. Helens is clear of UV-absorbing aerosol, while the smoke over Canada is just west of the position for May 18, 1980. On May 18 the ash cloud and Canadian smoke are clearly visible (both drifting eastward) and clouds of westward drifting dust over Florida (originating in Africa) and over Texas moving northward and westward. The absorbing aerosol features over New Mexico, Arizona, Nevada, and California on May 19 and 20 appear to be associated with the dust cloud over Mexico and Texas on May 18 and 19. Examination of the 380 nm reflectivity data shows that there was no significant cloudiness from the western coast of Mexico to the Atlantic Ocean east of Florida on May 18, 19, and 20 that might obscure the dust plume observations. May 17 had clouds off northwestern Florida and Louisiana but not near Texas or eastern Florida. The 380 nm reflectivity showed that May 17 had significant cloud cover over the central United States and May 18 over the eastern United States that does not appear in the residue images. It should be noted that Mexico has small sources of dust that appear to be located near the New Mexico border in Chihuahua (31°N 106.9°W) and in Coahuila (26.3°N 103.1°W). The existence of dust plumes on these days has not been validated by other independent data.

On May 18, volcanic SO_2 is not visible in the gridded TOMS data used in Figure 3 but is visible in the original higher resolution, 50 km × 50 km, scan data because only a small amount of SO_2 has formed in the first few hours before the TOMS observation. On the following day, May 19, the SO_2 cloud (contour lines) is clearly visible near the lower-latitude ash cloud. Part of the original ash cloud split off and followed a more northern trajectory. This is the result of wind shear at different altitudes similar to that estimated by trajectory analysis for the El Chichon eruption [*Seftor et al.*, 1996] or for the South American biomass burning [*Hsu et al.*, 1996]. The north-

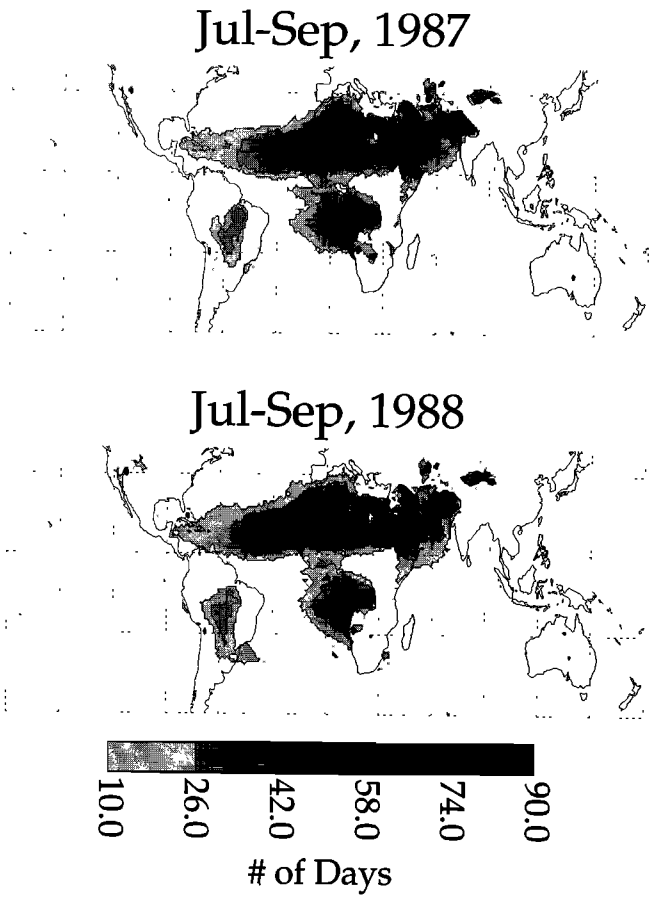

Figure 4. Maps of UV-absorbing aerosol occurrence during northern hemisphere summer months (July, August, September 1987 and 1988).

eastern trajectory of the ash cloud was at about 2 to 3 km altitude, while the southeastern ash cloud and SO_2 were carried by winds at about 8–12 km altitude [*Chung et al.*, 1981]. On May 20 the volcanic ash continues southeastward accompanied by the SO_2 cloud, while the northern ash cloud moves almost due east.

The UV-absorbing aerosol feature over Texas and Mexico on May 18 and 19 is probably only dust because there is no known large-scale fire in that region. There are frequently occurring source regions in Mexico for absorbing aerosols, two of which are located at 26.5°N 103°W in a mountain region and at 31°N 107°W, a dry lake bed just south of El Paso. Motion of the Texas/Mexico aerosol feature is consistent with the winds in the area. Similar features are seen in other years over Mexico, Texas, and the U.S. Southwest.

The accuracy of the TOMS calibration is sufficient for detection of UV-absorbing aerosols from the entire 1979 to 1993 data record as well as the Meteor 3/TOMS data record (1991–1994). For Nimbus 7/TOMS, there may be a small instrumental drift in the N-value residue data starting in 1990 related to problems in the synchronization of the chopper motor with the photon-counting electronics. The error is too small to affect ozone trend calculations. In this paper, aerosol trends will be examined only during the most stable period of TOMS operation and calibration, from 1984 to 1989. Outside of this period, ΔN_{340} from UV-absorbing aerosols can easily be detected and its relative strength observed. However, the variation between different years (1979–1983 and 1990–1993) contains instrumental components that may affect the detection of small trends in UV-absorbing aerosol amounts. Except for South American biomass burning, trends in aerosol amounts appear to be much smaller than the interannual variability and so are not statistically significant.

Occurrence of UV-Absorbing Aerosols

The largest sources of UV-absorbing aerosols in the atmosphere are from biomass burning and wind-borne desert dust from events that last a week or longer. Since most biomass burning is from deforestation or agricultural practices, the events have a frequency of occurrence that is tied to the dry seasons in each region. In the case of biomass burning in agricultural regions (e.g., South America, Africa, China, Indonesia) the start and duration of the burning is controlled by local crop requirements. Many of these fires are reset daily during the dry season and die down during the night. The largest contributor to atmospheric smoke outside of dry-season burning originates in the large consumption of coal in northeastern China beginning in winter and continuing into early spring. The smaller and shorter duration events are "natural events" frequently caused by lightning that occur during the driest months (for example, in Canada and the United States; see Figures 2 and 3). The majority of desert dust originates at the latitude of the Sahara and Sahel regions (near 10°N–28°N) and in a belt stretching from the western coast of Africa to central Asia (Arabian Peninsula, northern India, Tarim Basin, and Takla Maken Desert, 40°N 80°E, in China). During the summer months, dust is observed daily for periods of a week to several months. Smaller dust and smoke events originate at other locations (e.g., dust in southern Australia and smoke and dust in the western United States).

Figure 4 shows the number of days that the UV-absorbing aerosols were observed with $\Delta N_{340} > 1$ in the TOMS data between the latitudes of ±50° during the months of July, August, and September 1987 and 1988. The scale is chosen so that only major sources show in the figure (a minimum of 10 days out of 90 days). The most prominent feature is caused by the desert dust storms coming off the Saharan and Sahel regions and reaching across the Atlantic over the Caribbean and on some days into the Gulf of Mexico. The dust is observed over large areas of the Atlantic Ocean for more than 45 days out of 90. During these 3 months in 1987, dust was observed every day over portions of the Sahara and Sahel regions and the Arabian Peninsula. A smaller region of desert dust is from the Thar Desert in India and Pakistan. Smaller features are observable within the main dust cloud that are associated with well-defined geographic features. One of the most prominent of these is a large dry lake bed in the Sahel region of Africa near Lake Chad (13.5°N, 14°E). Another is the clearly defined shape of the mountainous region forming the northern border of India with dust visible just to its south (see Figure 5) for most of May 1984.

Farther south, there is a strong biomass burning signal centered in Angola on the west coast of southern Africa that is transported over the Atlantic Ocean at the same time biomass burning smoke occurs from a source of shorter duration in Brazil, Uruguay, Paraguay, and Argentina. There are smoke traces that can be seen on many days coming off the coast of Peru over the Pacific Ocean and off the coast of Argentina over the Atlantic Ocean following persistent wind trajectories

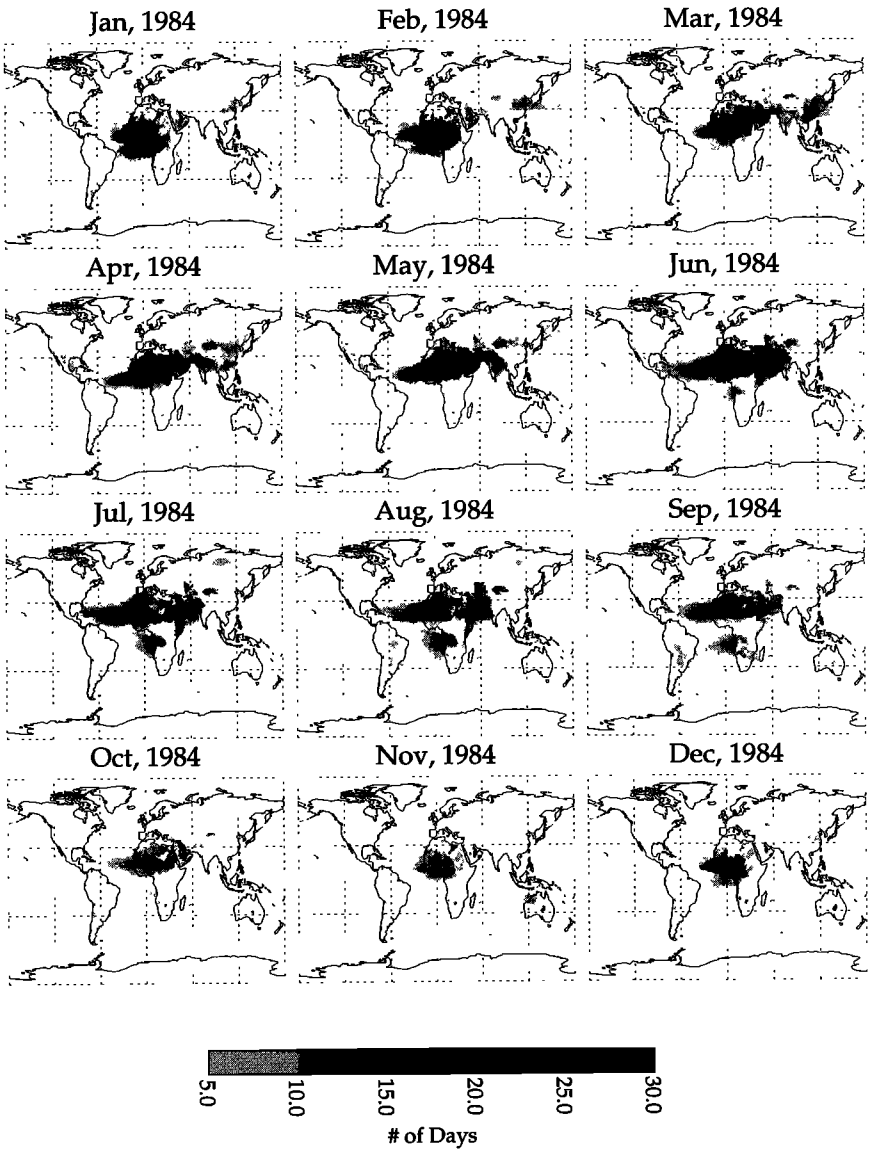

Figure 5. Monthly maps of UV-absorbing aerosol occurrences lasting more than 5 days for 1984.

in the lower troposphere [*Hsu et al.*, 1996]. A similar observation applies to the smoke traces originating in Zambia and Zimbabwe and observed off the east coast of southern Africa over the Indian Ocean (see Figure 2).

Small sources of dust are identifiable in magnified images of Figures 5 and 6. The monthly maps show a dust source in the coastal regions of Oman centered on 18.7°N, 56.4°E that persists throughout the year and extends southward into Yemen. A similarly persistent dust source occurs farther to the north in Saudi Arabia and Qatar near the Persian Gulf. Both of these sources reach maximum intensity in June and July and begin to subside in August. At their maximum they cover most of the Arabian Peninsula. A weak intermittent dust source occurs during some years (e.g., 1988) near the Aral Sea (an inland salt sea) in Uzbekistan and Kazakhstan possibly arising from the dry area that was part of its sea bed. The Aral Sea dust was seen mainly in February and again in September. A small dust source appears in Australia from December to April from Lake Eyre (28°S 137.2°E) (a salt lake) that is often dry during the summer.

As suggested by J. M. Prospero (private communication, 1996) many dust sources in the TOMS images can be associated with dry lake beds or intermittently dry rivers where the soil is frequently disturbed for agricultural purposes during the wet season and then becomes airborne during the dry season. For example, areas of agricultural activity appear to be associated with some of the dust activity in the Sahel region especially near Lake Chad. It does not appear that agricultural activity is associated with the weak dust source near Lake Eyre in Australia. The weak Aral Sea dust source may be related to its shrinking area from diversion of water for irrigation. In addition to the drought cycle, there may be an anthropogenic component for the largest dust sources (e.g., the Sahel) and certainly for the biomass burning smoke sources (e.g., western Africa). Many sandy desert areas contain particulates that are larger than the dry-lake bed soils and so do not remain airborne for long periods or become transported over large distances. In addition, sandy particles that are not lifted out of the boundary layer would not be visible to TOMS as an absorbing aerosol embedded in a Rayleigh atmosphere.

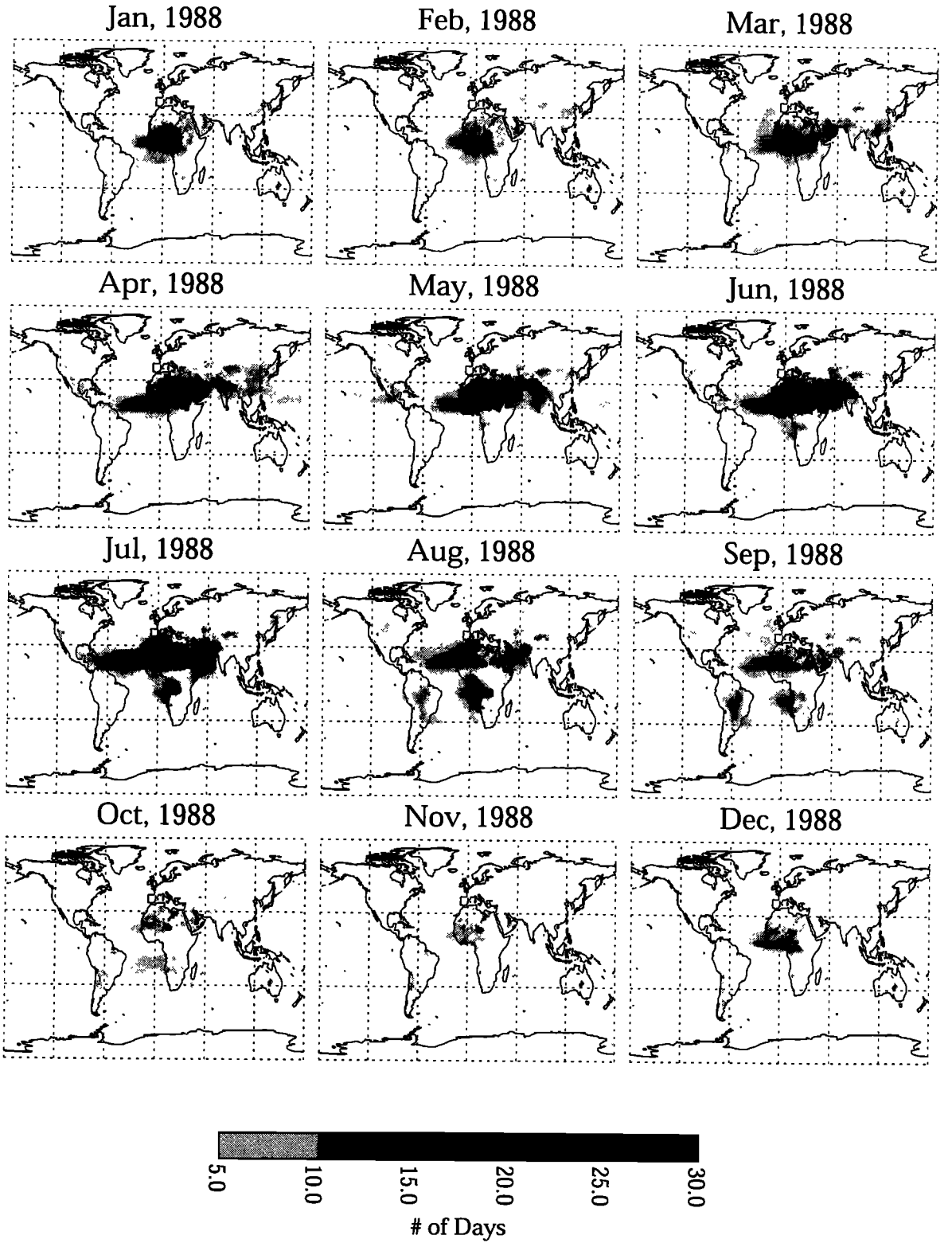

Figure 6. Monthly maps of UV-absorbing aerosol occurrences lasting more than 5 days for 1988.

Time Series

Each of the major sources of atmospheric UV-absorbing aerosols observed by TOMS is linked to a natural or anthropogenic cause and has an annual cycle. The major sources are desert dust originating in a latitude band 20°N ± 15° (e.g., African Saharan Desert and Sahel region, Arabian Peninsula, Indian Thar Desert, and northern border region), biomass burning (e.g., equatorial central South America, equatorial western Africa, western midlatitude Africa, southeastern China, and Indochina), and possible mixture of coal smoke and dust (e.g., northern China). Smaller sources observed by TOMS are dust from the Tarim Basin and Takla Maken

Desert (40°N 80°E in western China), dust from central Australia (Lake Eyre region), biomass burning in Canada, Indonesia, etc., volcanic eruptions (Mount Pinatubo, Philippines, 1991; El Chichon, Mexico, 1982; Mount St. Helens, United States, 1980), and single-occurrence events (e.g., Kuwait oil fire). Except for the largest volcanic eruptions, all of the other sources of UV-absorbing aerosols inject most of the particulates into the lower atmosphere between 0 km and 15 km with the majority of the dust below 10 km. Smoke is typically at lower altitudes, 4 km or below; desert dust is at low altitudes near its source, but can rise in regions of upward convection, and is observed at low altitudes (1 km to 4 km) as the dust crosses the Atlantic Ocean [*Prospero and Carlson*, 1972; *Carlson and Prospero*, 1972]. In all cases the injected UV-absorbing aerosols follow the regional prevailing winds and cover areas much bigger than their sources.

Figures 5 and 6 show monthly UV-absorbing aerosol occurrence graphs (number of days in a month during the years 1984 and 1988) for events lasting at least 5 days per month (dpm) for each 1° × 1.25° pixel on the world map. The main features occur annually with the minimum amount of global UV-absorbing aerosol during October to November and the maximum amount during June to July. Starting in November, there is a small amount of biomass burning in equatorial western Africa and only a small amount of desert dust from the Sahel region. As can be seen in Figures 5 and 6, the equatorial western Africa biomass burning increases during December and January. Also from December to April, there is coal burning activity in northern China that may be mixed with dust and transported eastward over the Pacific Ocean and the southern portions of Japan. Unlike volcanic eruptions (see Figure 3), there was insufficient SO_2 associated with the coal burning in China to be observed by TOMS. During March and April there is additional smoke from southeastern China and Indochina caused by agricultural burning prior to the spring planting. During January, February, and March there is agricultural burning in western equatorial Africa intermixed with some desert dust. In some years (e.g., 1988; see Figure 6, March), dust blows northward over the ocean toward Spain for 5–15 dpm. Smoke appears in South America for 5–15 dpm during August and September with a small additional amount of burning in October in the region around the mouth of the Amazon River due to agricultural activities [*Setzer and Pereira*, 1991].

Starting in March and April, the desert dust appears in northern India just south of the Himalayan Mountains on the border with China. In April and May (see Figures 5 and 6) the 30 dpm spatial distribution of dust follows the shape of the mountain chain. For 5–10 dpm, dust appears over most of India and spreads over the Bay of Bengal and into the Arabian Sea. Starting in March, 30 dpm dust appears over the eastern portion of the Arabian Peninsula and 20–25 dpm dust appears over portions of the Sahara and Sahel. During the following few months the amount of dust increases and extends across the Atlantic Ocean to Florida and Cuba. After July the amount of dust diminishes rapidly each month until the minimum in October and November.

Both the time series and the occurrence maps show a clear increase in the amount and duration of the South American biomass burning for the period since the beginning of TOMS data in 1978. For central South America, TOMS data indicate that the peak months for smoke are during the middle of the dry season in August and September. The TOMS observations should be a good measure of biomass burning because they are

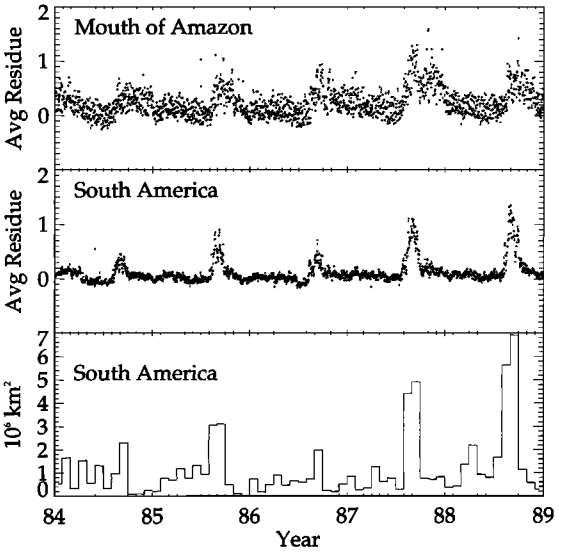

Figure 7. Time series (1984–1988) for the occurrence of biomass burning in central South America from 0° to 20°S latitude and near the mouth of the Amazon River. The bottom panel gives an estimate of the total area covered over both land and ocean for all of South American burning.

obtained near local noontime which is within the daily peak period for burning (1130 to 1430), while 3 to 6 hours later the activity could be 2 to 20 times less [*Prins and Menzel*, 1994]. The area observed by TOMS to be covered with smoke has increased from about 1 million km^2 in 1984 to over 6 million km^2 by 1988 (see Figure 7) with no further systematic increase to the end of the TOMS data record in 1993. Similarly, the number of days per month that smoke was observed grew from 5–15 dpm in 1984 to 10–25 dpm by 1988. A similar observation was made from the GOES visible-infrared spin-scan radiometer where the estimated amount of burning nearly doubled from 1983 to 1991 [*Prins and Menzel*, 1994].

There is a similar occurrence of biomass burning for Africa in July, August, and September at the same latitudes [*Cros et al.*, 1991]. Unlike the South American burning, African burning centered at 13°S shows no systematic increase on top of the annual variability (see Figure 8). For example, in South America there was a sharp drop in observed biomass burning smoke in 1989 caused by an exceptionally wet year (short dry season). The magnitude of the decrease is larger than the interannual error estimates for the data after 1988.

The persistent features shown in Figures 5 and 6 are the major contributors to the atmospheric burden of UV-absorbing aerosols in contrast to the more transient features shown in Figures 2 and 3. With minor variations, these features occur every year with fluctuations in strength and area that are small fractions about their mean values. The mean and standard deviation for each 1° × 1.25° pixel have been computed for each monthly map for the 5 years 1984–1989. During the peak months for biomass burning and desert dust the standard deviation is 1 dpm in the densest regions of UV-absorbing aerosols (25–30 dpm) and about 5 dpm in the regions where the occurrence is 10–15 dpm. An exception is in central South America where the annual increase in biomass burning leads to a standard deviation of 4–8 dpm within the region of maximum observed smoke. The largest variability is associated with changes in the amount of rainfall.

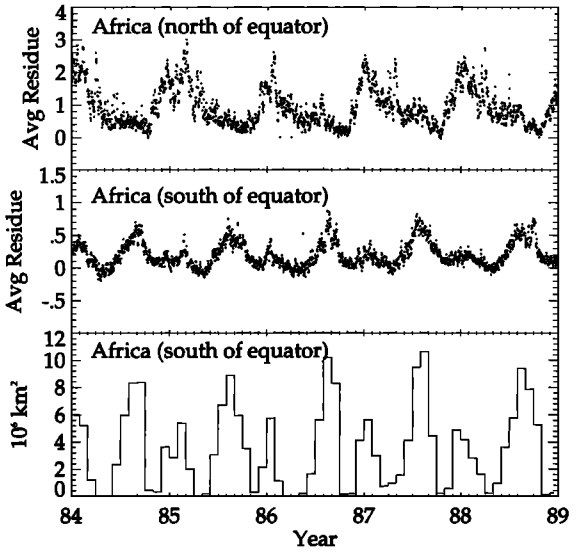

Figure 8. Time series (1984–1988) for the occurrence of biomass burning in Africa. The areas covered are in two boxes from 0° to 10°N, 15°W–20°E for the top panel, and 0°–35°S, 10°E–40°E for the middle and bottom panels. The bottom panel gives an estimate of the total area covered over both land and ocean.

Figures 7–10 show time series of the daily N-value residue, ΔN_{340}, for different locations associated with the major sources of UV-absorbing aerosols. In each case, a daily average value of ΔN_{340} is obtained within a latitude by longitude box constructed to contain data from the indicated event over both land and ocean. These figures show that the UV-absorbing aerosol signal stands out clearly from the signal at other times of the year that do not have significant amounts of absorbing aerosols. The conversion of given values of ΔN_{340} into optical depth for different types of events cannot be directly compared because of the strong dependence on particle size, refractive index, and aerosol-cloud height. For example, the larger particles typical of desert dust have a larger ΔN_{340} than the smaller particles typical of smoke for the same optical depth (see Table 1 for the relationship between aerosol particle size r_{eff}, absorption index k, aerosol cloud height h, and optical depth τ_{380}).

The amount of biomass burning in South America shows an increase in amount and area covered over the years represented in Figure 7. In subsequent years (1990 to 1992) the amount remains near the 1988 levels with some interannual variability. As mentioned earlier, TOMS had minor calibration problems after 1990, so that the relative values of ΔN_{340} may not be accurate at the 0.1% level. South America is the only example of long-term increase over the years covered by TOMS data (1979 to 1992). As can be seen from the middle and upper panels, there is a strong seasonal component with burning starting in July and dying out in October. A similar pattern is repeated for the much smaller Amazon River basin region but with indication of smaller amounts of burning during other months.

The western African biomass burning in a latitude by longitude box, 0° to 35°S, 10°E–40°E, starts with the dry season in June and continues until September (see Figure 8). The secondary peak occurring each year during January is from biomass burning occurring slightly north of the equator (0°–10°N, 15°W–20°E) and transported southward by the prevailing winds. The secondary midyear peaks north of the equator are caused by the southward transport of desert dust originating in the Sahara and Sahel. The January biomass burning peaks are not significantly contaminated with desert dust as this period is close to the minimum amount of African dust in the atmosphere (see Figure 9). There is no apparent trend shown in the amount of biomass burning (Figure 8) or in the area covered by the smoke.

The main source of atmospheric desert dust originates from a band stretching from near the west coast of Africa to India approximately in the 10°N–28°N latitude band (see Figures 5 and 6). Dust blows for most of the year except for the months of December and January. The maximum amount of dust occurs during the May to June period in both amount and area

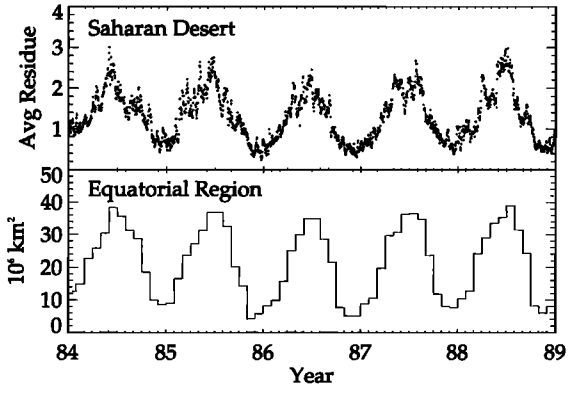

Figure 9. Time series (1984–1988) for the occurrence of desert dust originating in the Saharan Desert and Sahel regions from 15°N to 30°N, 15°W–20°E. The bottom panel gives an estimate of the total area covered over both land and ocean for dust originating in the Saharan Desert and Sahel regions, Arabian Peninsula, and India.

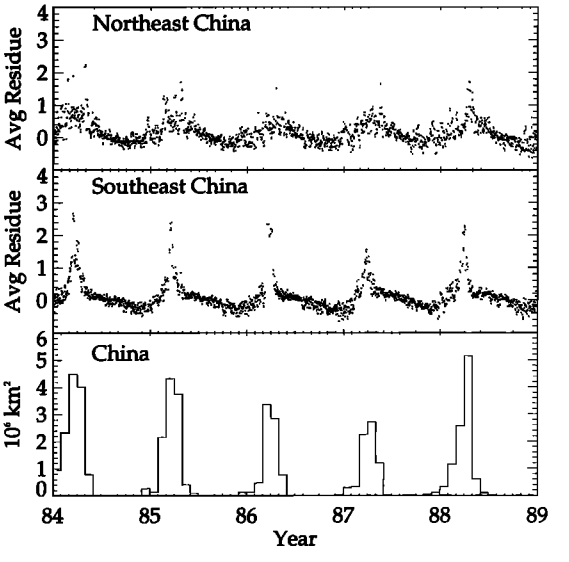

Figure 10. Time series (1984–1988) for the occurrence of coal burning smoke mixed with dust in northeastern China (32°N–42°N, 110°E–121°E) and for the occurrence of agricultural biomass burning in southeastern China (20°N–30°N, 110°E–122°E). The bottom panel gives an estimate of the total area covered over both land and ocean.

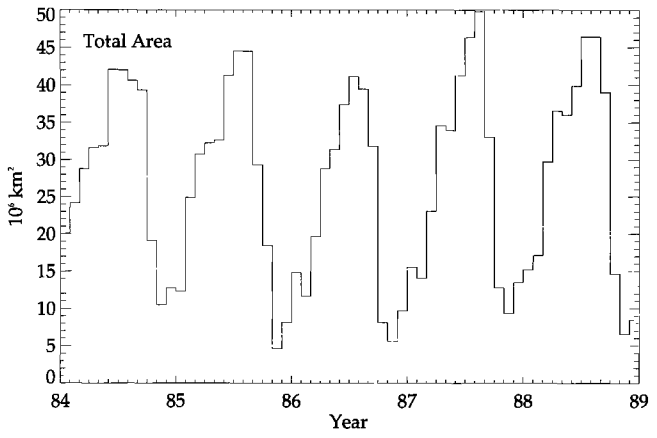

Figure 11. Sum of areas covered by UV-absorbing aerosols from all of the major sources.

covered. The dust covers far more area than smoke from biomass burning (peaking at 35×10^6 km^2 compared with 3×10^6 km^2 for African smoke and 4×10^6 km^2 for South American smoke), with the dust extending across the Atlantic Ocean, Cuba, and Florida.

A major source of UV-absorbing aerosols over China occurs in the northeast during January to May (see Figure 10) that could include smoke from coal burning when it is lifted above the low level inversion layer during the spring. In the spring there are vigorous frontal passages at times corresponding to the spring peak in ΔN_{340} that mix aerosols to higher altitudes and generate dust clouds [*Husar et al.*, this issue; J. M. Prospero, private communication, 1996). The resulting dust and smoke blow eastward over Japan and Korea. Both the magnitude of ΔN_{340} and the area covered by dust and coal smoke are smaller than ΔN_{340} from biomass burning smoke occurring during March and April in southeastern China and Indochina.

The total area of the Earth's surface covered by UV-absorbing aerosols observed by TOMS over the course of a year, with a minimum observable optical depth of at least 0.1, is about 53 million km^2 with small variations between years (covering approximately 10% of the Earth's surface). The area covered during each month is shown in Figure 11. The maximum area covered at one time (mostly dust) is about 42 ± 5 million km^2 with a maximum during 1987 of 50 million km^2. Most of these absorbing aerosols are observed at altitudes above 2 km where they are transported over large distances by the prevailing winds. Absorbing aerosols contained in the boundary layer are not seen by TOMS and are not included in the above estimate of areal cover.

Conclusion

Global observations of the major sources of atmospheric UV-absorbing aerosols from biomass burning and desert dust show that a significant portion of the Earth's surface is affected for at least 11 months of the year with reduced amounts during the other month. The minimum UV-absorbing aerosol content occurs in late October to November and the maximum during June and July for most years. The area covered amounts to about 53 million km^2 over land plus ocean during a year with about 42 ± 5 million km^2 covered at the same time during June and July (see Figure 11). During the months of maximum smoke and dust, UV-absorbing aerosols with an optical depth of at least 0.1 cover about 10% of the Earth's surface. Detection of absorbing aerosols and calculation of optical depths is limited by the presence of large-scale and subpixel clouds in the TOMS field of view.

The accuracy of the entire 14.5 years of TOMS reflectivity data currently does not permit long-term trends of UV-absorbing aerosols to be determined with confidence outside of the 1984 to 1989 time period. During the period from 1984 to 1989, only the central South American region showed a clear increase in the rate of production of UV-absorbing aerosols. In other major production regions, there are single years of increased aerosol production but no apparent trends. There is significant year-to-year variability of UV-absorbing aerosol amounts and area covered from major aerosol source regions: (1) central South America near 10°S latitude; (2) Africa near 0°–20°S and 0°–10°N latitude; (3) Saharan Desert and Sahel region, Arabian Peninsula, and northern India near 25°N latitude; (4) agricultural burning in Indonesia, southeastern China and Indochina, and near the mouth of the Amazon River; and (5) dust and coal burning in northeastern China. Unlike the sources for desert dust, biomass burning regions show much larger variability than average whenever there is an exceptionally wet year. The first three of the major aerosol source regions dominate the injection of UV-absorbing aerosols into the atmosphere each year and cover areas far outside of their source regions. Some of the sources of dust seen in the TOMS images appear to be associated with intermittently dry rivers, lake beds, or low-lying drainage areas (J. M. Prospero, private communication, 1996). Since many of these are also regions of intensive agriculture (particularly the Sahel near Lake Chad), there may be an anthropogenic component in the amount of dust injected into the atmosphere each year in addition to that caused by the drought cycle.

Other sources of UV-absorbing aerosol production are observed in the TOMS data from 1979 to 1993. Most prominent among these are volcanic eruptions (El Chichon, Mount St. Helens, Mount Pinatubo), United States and Canadian forest and brush fires, and smaller desert dust injections (Tarim Basin and Takla Maken Desert in western China, Lake Eyre in central Australia, and in the U.S. Southwest). The smallest sources observed by TOMS are one-time events that persist for 1 day to a few months (e.g., Kuwait oil fire, Yellowstone Park fire, 1980 dust cloud over southern Texas, Russian Siberian fire). Sources arising from urban and industrial emissions are not of sufficient amount or cover enough area to be routinely seen in the TOMS reflectivity data. The 50 km × 50 km (100 km × 100 km side-scan average) nadir-view spatial resolution of Nimbus 7/TOMS is not sufficient to see UV-absorbing aerosols over cities. UV-absorbing aerosols are occasionally seen over the Atlantic Ocean near the southeastern coast of the United States. Some of these have been traced to their source in the African dust regions using TOMS data.

References

Ardanuy, P. E., L. Kyle, and D. Hoyt, Global relationships among the earth's radiation budget, cloudiness, volcanic aerosols, and surface temperatures, *J. Clim.*, *5*, 1120–1139, 1992.

Bhartia, P. K., J. Herman, R. D. McPeters, and O. Torres, Effect of Mount Pinatubo aerosols on total ozone measurements from backscatter ultraviolet (BUV) experiments, *J. Geophys. Res.*, *98*, 18,547–18,554, 1993.

Bodhaine, B. A., Aerosol absorption measurements at Barrow, Mauna Loa, and the south pole, *J. Geophys. Res.*, *100*, 8967–8975, 1995.

Carlson, T. N., and J. M. Prospero, The large scale movement of Saharan air outbreaks over the equatorial North Atlantic, *J. Appl. Meteorol.*, *11*, 283, 1972.

Cros, B., D. Nganga, R. A. Delmas, and J. Fontan, Tropospheric ozone and biomass burning in intertropical Africa, MIT Press, Cambridge, Mass., 1991.

Chung, Y. S., A. Gallant, F. Fanaki, and M. Millan, On the observations of Mount St. Helens volcanic emissions, *Atmos. Ocean*, *19*, 172–178, 1981.

D'Almeida, G. A., On the variability of desert aerosol radiative characteristics, *J. Geophys. Res.*, *92*, 3017–3026, 1987.

Dave, J. V., Multiple scattering in a non-homogeneous, Rayleigh atmosphere, *J. Atmos. Sci.*, *22*, 273–279, 1965.

Dave, J. V., Effect of aerosols on the estimation of total ozone in an atmospheric column from the measurement of its ultraviolet radiance, *J. Atmos. Sci.*, *35*, 899–911, 1978.

Eck, T. F., P. K. Bhartia, P. H. Hwang, and L. L. Stowe, Reflectivity of the Earth's surface and clouds in ultraviolet from satellite observations, *J. Geophys. Res.*, *92*, 4287–4296, 1987.

Haywood, J. M., and K. P. Shine, The effect of anthropogenic sulfate and soot aerosol on the clear sky planetary radiation budget, *Geophys. Res. Lett.*, *22*, 603–606, 1995.

Heath, D. F., A. J. Krueger, H. R. Roeder, and B. D. Henderson, The solar backscatter ultraviolet and total ozone mapping spectrometer (SBUV/TOMS) for Nimbus G, *Opt. Eng.*, *14*, 323–331, 1975.

Herman, J. R., and D. Larko, Low ozone amounts during 1992–1993 from Nimbus 7 and Meteor 3 total ozone mapping spectrometer, *J. Geophys. Res.*, *99*, 3483–3496, 1994.

Herman, J. R., P. K. Bhartia, J. Ziemke, Z. Ahmad, and D. Larko, UV-B increases (1979–1992) from decreases on total ozone, *Geophys. Res. Lett.*, *23*, 2117–2120, 1996.

Holben, B., T. F. Eck, and R. S. Fraser, Temporal and spatial variability of aerosol optical depth in the Sahel region in relation to vegetation remote sensing, *Int. J. Remote Sens.*, *12*, 1147–1163, 1991.

Hsu, N. C., J. R. Herman, P. K. Bhartia, C. J. Seftor, O. Torres, A. M. Thompson, J. F. Gleason, T. F. Eck, and B. N. Holben, Detection of biomass burning smoke from TOMS measurements, *Geophys. Res. Lett.*, *23*, 745–748, 1996.

Husar, R. B., J. M. Prospero, and L. L. Stowe, Characterization of tropospheric aerosols over the oceans with the NOAA advanced very high resolution radiometer optical thickness operational product, *J. Geophys. Res.*, this issue.

Joiner, J., P. K. Bhartia, R. P. Cebula, E. Hilsenrath, R. McPeters, and H. Park, Rotational raman scattering (Ring effect) in satellite backscatter ultraviolet measurements, *Appl. Opt.*, *34*, 4513–4525, 1995.

Kaufman, Y. J., et al., Biomass Burning Airborne and Spaceborne Experiment in the Amazon (BASE A), *J. Geophys. Res.*, *97*, 14,581–14,599, 1992.

Krueger, A. J., L. S. Walter, P. K. Bhartia, C. C. Schnetzler, N. A. Krotkov, I. Sprod, and G. J. S. Bluth, Volcanic sulfur dioxide measurements from the total ozone mapping spectrometer instruments, *J. Geophys. Res.*, *100*, 14,057–14,076, 1995.

Matson, M., and B. Holben, Satellite detection of tropical burning in Brazil, *Int. J. Remote Sens.*, *8*, 509–516, 1987.

McPeters, R. D., et al., Nimbus 7 total ozone mapping spectrometer (TOMS) data products users guide, *NASA Ref. Publ.*, *1384*, 1996.

Patterson, E. M., Measurements of the imaginary part of the refractive index between 300 and 700 nm for Mt. St. Helens ash, *Science*, *211*, 836–838, 1981.

Patterson, E. M., and C. K. McMahon, Absorption characteristics of forest fire particulate matter, *Atmos. Environ.*, *18*, 2541–2551, 1984.

Patterson, E. M., and C. O. Pollard, Optical properties of the ash from El Chichon volcano, *Geophys. Res. Lett.*, *10*, 317–320, 1983.

Patterson, E. M., D. A. Gillette, and B. H. Stockton, Complex index of refraction between 300 and 700 nm for Saharan aerosols, *J. Geophys. Res.*, *82*, 3153–3160, 1977.

Prins, E. M., and W. P. Menzel, Geostationary satellite detection of biomass burning in South America, *Int. J. Remote Sens.*, *13*, 2783–2799, 1992.

Prins, E. M., and W. P. Menzel, Trends in South American biomass burning detected with the GOES visible infrared spin scan radiometer atmospheric sounder from 1983 to 1991, *J. Geophys. Res.*, *99*, 16,719–16,735, 1994.

Prospero, J. M., and T. N. Carlson, Vertical and areal distribution of Saharan dust over the western equatorial north Atlantic Ocean, *J. Geophys. Res.*, *77*, 5255–5265, 1972.

Robinson, D. A., Problems in global fire evaluation: Is remote sensing the solution, in *Global Biomass Burning: Atmospheric, Climatic and Biospheric Implication*, MIT Press, Cambridge, Mass., 1991.

Seftor, C. J., N. C. Hsu, J. R. Herman, P. K. Bhartia, O. Torres, W. I. Rose, D. J. Schneider, and N. Krotkov, Detection of volcanic ash clouds from Nimbus 7/TOMS reflectivity data, *J. Geophys. Res.*, in press, 1996.

Setzer, A. W., and M. C. Pereira, Amazon biomass burnings in 1987 and their tropospheric emissions, *Ambio*, *20*, 19–20, 1991.

Stowe, L. L., C. G. Wellemeyer, T. F. Eck, H. Y. M. Yeh, P. H. Hwang, H. L. Kyle, P. Pellegrino, P. K. Bhartia, and C. S. Long, Nimbus-7 global cloud climatology, I, Algorithm and validation, *J. Clim.*, *1*, 447, 1985.

Torres, O., J. R. Herman, P. K. Bhartia, and Z. Ahmad, Properties of the Mt. Pinatubo aerosols as derived from Nimbus 7 total ozone mapping spectrometer measurements, *J. Geophys. Res.*, *100*, 14,043–14,055, 1995.

Wen, S., and W. I. Rose, Retrieval of sizes and total masses of particles in volcanic clouds using AVHRR bands 4 and 5, *J. Geophys. Res.*, *99*, 5421–5431, 1994.

Westphal, D. L., and O. B. Toon, Simulations of microphysical, radiative and dynamical processes in a continental-scale forest fire smoke plume, *J. Geophys. Res.*, *96*, 22,379–22,400, 1991.

Westphal, D. L., O. B. Toon, and W. R. McKie, Atmospheric effects of a Canadian forest fire smoke plume, IRS'88, in *Current Problems in Atmospheric Radiation*, A. Deepak, Hampton, Va., 1989.

P. K. Bhartia and J. R. Herman, Laboratory for Atmospheres, NASA GSFC, Code 916, Greenbelt, MD 20771.

E. Celarier, Software Corporation of America, 4601 Presidents Drive, Lanham, MD 20706-4365.

C. Hsu, C. Seftor, and O. Torres, Hughes STX Corporation, 7701 Greenbelt Road, Greenbelt, MD 20770.

(Received August 12, 1996; revised November 8, 1996; accepted November 8, 1996.)